Check for updates

Special Issue – Advective disturbances in combustor thermoacoustics

International journal of spray and combustion dynamics

International Journal of Spray and Combustion Dynamics
0(0) 1–15
© The Author(s) 2017
Reprints and permissions:
sagepub.co.uk/journalsPermissions.nav
DOI: 10.1177/1756827717740775
journals.sagepub.com/home/scd
SAGE

Large-Eddy-simulation prediction of indirect combustion noise in the entropy wave generator experiment

Stéphane Moreau[1], C. Becerril[2] and L.Y.M Gicquel[2]

Abstract

Compact and non-compact analytical solutions of the subsonic operating point of the entropy wave generator experiment are compared with detailed numerical results obtained by large Eddy simulations. Two energy deposition methods are presented to account for the experimental ignition sequence and geometry: a single-block deposition as previously used and a delayed deposition that reproduces the experimental protocle closely. The unknown inlet acoustic reflection coefficient is assumed to be fully reflective to be more physically consistent with the actual experimental setup. The time delay between the activation of the heating modules must be considered to retrieve the temperature signal measured at the vibrometer and pressure signals at the microphones. Moreover, pressure signals extracted from the large Eddy simulations in the outlet duct using the delayed ignition model clearly reproduce the experimental signals better than the analytical models. An additional simulation with actual temperature fluctuations directly injected at the inlet of the computational domain clearly shows that the pressure fluctuations produced by the acceleration of the hot slug yields indirect noise almost entirely. Finally, the entropy spot is shown to be distorted when convecting through the turbulent flow in the entropy wave generator nozzle. Its amplitude decreases and its shape is dispersed, but hardly any dissipation occurs. The distortion appears to be negligible through the nozzle and become important only when convected over a long distance in the downstream duct. As the dominant frequencies of the entropy wave generator entropy forcing are very low, the effects of dispersion by the mean flow are however weak.

Keywords

Nozzle flow, combustion noise, large Eddy simulation

Date received: 27 April 2017; accepted: 11 October 2017

1. Introduction

Modern turboengine architectures involve lean, partially premixed and more unstable combustors,[1] along with fewer turbine stages to prevent the propagation of combustion noise outside of the engine.[2] Similarly, turboshaft engines have even fewer turbine stages and lower ejection velocity and consequently no jet noise to mask the combustion noise.[3,4] As a result of such technological changes, the latter noise source is becoming a major nuisance that needs to be understood and controlled to meet future regulations. Two noise mechanisms are usually evoked: a direct combustion noise caused by the fluctuations of the flame heat release,[5] and an indirect combustion noise mostly caused by the acceleration of entropy spots,[6] which could not be experimentally evidenced until recently. Indeed an experiment at the German Aerospace Center DLR termed entropy wave generator (EWG) was specifically designed to study the latter, and was the first to conclusively show the generation of indirect noise that eluded the community for several decades.[7,8]

Two EWG reference cases have been considered since then: a supersonic case (case 1) where the nozzle throat is choked and a shock wave is present in the

[1]Département de Génie Mécanique, Université de Sherbrooke, Sherbrooke, QC, Canada
[2]Cerfacs, Toulouse, France

Corresponding author:
Stéphane Moreau, Département de Génie Mécanique, Université de Sherbrooke, 2500 bd de l'université, J1K 2R1, Sherbrooke, QC, Canada.
Email: stephane.smoreau@usherbrooke.ca

Creative Commons CC BY-NC: This article is distributed under the terms of the Creative Commons Attribution-NonCommercial 4.0 License (http://www.creativecommons.org/licenses/by-nc/4.0/) which permits non-commercial use, reproduction and distribution of the work without further permission provided the original work is attributed as specified on the SAGE and Open Access pages (https://us.sagepub.com/en-us/nam/open-access-at-sage).

diverging section and a subsonic case (case 2) for which the Mach number at the nozzle throat $M_{N_{th}}$ is high enough to observe the saturation of indirect noise ($M_{N_{th}} = 0.7$). Eventhough the supersonic case has been modeled and simulated with success,[9,10] all results converging to a compact nozzle for which the indirect noise dominates, the subsonic case has not been fully understood yet, and no detailed turbulent simulations have been achieved so far. Even the ratio of direct to indirect noise is still a matter of controversy: the analytical predictions of Duran et al.[11] suggest more direct noise from the heating device (HD) than indirect noise created at the nozzle throat, whereas unsteady Reynolds-Averaged Navier–Stokes (RANS) simulations by Muhlbauer et al.[12] and more recently Lourier et al.[13] suggest the opposite. Moreover only detailed turbulent simulations can adequately quantify the effects of dissipation and dispersion of a hot slug, as done by Morgans et al.,[14] Giusti et al.,[15] and Hosseinalipour et al.[16] in a simplified turbulent channel flow, or by Papadogiannis et al.[17] and Wang et al.[18] in a high-pressure turbine stage. Furthermore, the effects of turbulent mixing or flow separation on indirect combustion noise as described by Howe[19] can also be studied further within this specific numerical context. All of these effects have not been studied in previous EWG works, which are based on the coupling of RANS simulations with computational aeroacoustic (CAA) methodologies,[20,21] unsteady RANS simulations,[12,13] Euler simulations, and even analytical modeling.[9,11,22] To reach the need for higher-fidelity flow predictions, Large Eddy Simulation (LES) seems to be a first good candidate to simulate the high Reynolds number EWG subsonic test case, and provide further insight into the physical phenomena of indirect combustion noise generation and transmission.

First the EWG test facility and main data are outlined. The analytical method to model the EWG experiments that relies on the non-compact approach of Duran and Moreau[22] is then described with a particular emphasis on the improved HD model compared with Leyko et al's.[9] one. Preliminary results by Becerril et al.[23] have already shown its importance. Then the complete numerical strategy based on full 360° configurations of the EWG setup with and without exact or approximate energy deposition in the computational domain is presented. Conclusions are then drawn and the limitations of the analytical approach highlighted.

2. Entropy wave generator experiment

The complete domain of the EWG (illustrated in Figure 1) includes a settling chamber with a plate installed at the inlet to avoid the formation of the jet formed by the sudden expansion. In addition to the plate, a honeycomb flow straightener (hatched section in Figure 1) has been installed to minimize lateral velocity components and obtain a straight plug flow entering the nozzle. No experimental data on the inlet impedance are available and this parameter remains unknown.

A HD is placed in the duct upstream of the nozzle. This HD is composed of six modules themselves composed of electric resistances, each module being separated from its neighbors by $\Delta x_r = 8$ mm. The most upstream heating module is located at $x_{\mathrm{HD}_1} = -145.5$ mm from the nozzle throat. Note that experimentally a gap of 1.8 mm separates the electrical resistances from the duct wall to prevent overheating and fusion of the wires. This implies that only part of the boundary layer and flow is heated, an effect that has to be accounted for as accurately as possible in the LES. For the specific subsonic test case considered here, the temperature fluctuation is no longer measured by a thermocouple (local measurement) but by a vibrometer, which is a nonintrusive device that analyzes the change in the optical path length caused by the variation of flow density, and gives access to a temperature along a line of sight, here the duct diameter. Indeed once the HD is activated, a hot spot is convected and the temperature fluctuation produced by this energy deposition is measured by this vibrometer located at $x_{vib} = -58.5$ mm from the nozzle throat. Therefore,

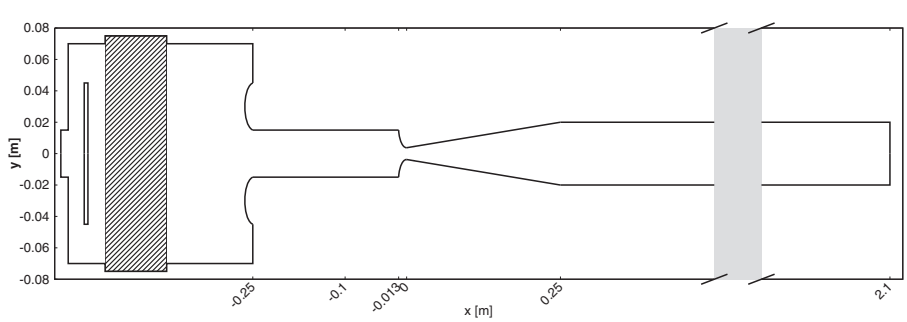

Figure 1. Sketch of the EWG complete geometry.

the temperature measured by this element can be described as a spatially-averaged temperature over the diameter

$$T_{vib} = T_{mean} = \frac{1}{2R}\int_{y=-R}^{R} T(y)\mathrm{d}y \tag{1}$$

After the HD, the flow enters the converging–diverging nozzle in which the flow is strongly accelerated. Downstream of the nozzle, in another tube section with a length of 1020mm and a diameter of 40mm, four wall-flushed microphones measure the pressure fluctuations induced by the acceleration of the entropy wave. The outlet impedance of the setup has been measured. More details on the experiment can be found in Bake et al.[8]

3. EWG analytical simulations

The analytical methodology proposed by Duran et al.[11] is here revisited by introducing a model that takes into account the entire HD and non-compact transfer functions of the nozzle. The model for the HD considers each heated ring of the device as a compact element. Therefore, each ring generates its own acoustic and entropy waves. Balance equations for mass-flow rate $\dot{m}$, total temperature T_t, and entropy s can hence be written for each compact heated ring

$$\left(\frac{\dot{m}'}{\dot{m}}\right)_{j,0} = \left(\frac{\dot{m}'}{\dot{m}}\right)_{j,1} \tag{2a}$$

$$\left(\frac{T_t'}{T_t}\right)_{j,0} + q_j'\left(1 + \frac{\gamma - 1}{2}M_0^2\right)^{-1} = \left(\frac{T_t'}{T_t}\right)_{j,1} \tag{2b}$$

$$\left(\frac{s'}{c_p}\right)_{j,0} + q_j' = \left(\frac{s'}{c_p}\right)_{j,1} \tag{2c}$$

where the prime corresponds to fluctuations, the subscript j indicates that the balance equation is applied to the jth ring, and subscripts 0 and 1 stand for upstream and downstream positions of the considered ring respectively. q_j' is the energy induced by the ring heating. γ and c_p are the air heat capacity ratio and the specific heat of air at constant pressure, respectively. M_0 is the inlet Mach number. Equations (2a), (2b), and (2c) are then introduced in the non-compact invariant formulation of Duran and Moreau.[22]

3.1. HD model

To reproduce the shape of the temperature fluctuation recorded by a thermocouple, while avoiding to simulate the activation sequence, Leyko et al.[9] introduced a function ξ of time t using two exponentials. The stiffness of the rising and decreasing phases of the respective functions was controlled with a single relaxation parameter noted τ. In the present study, which follows the same strategy, one relaxation coefficient is used for the rising phase τ_1 and a second one for the decreasing phase τ_2

$$\xi(t) = \begin{cases} 0 & \text{if } t < t_0, \\ 1 - \exp\left(-\frac{t-t_0}{\tau_1}\right) & \text{if } t \in \left[t_0; t_0 + T_p\right] \\ \left[1 - \exp(-\frac{T_p}{\tau_1})\right]\exp(\frac{t_0 - t + T_p}{\tau_2}) & \text{if } t > t_0 + T_p \end{cases} \tag{3}$$

where t_0 is the triggering time of the HD ignition sequence and T_p is the pulse duration or the duration of the energy deposition. As $\Delta T_{exp}\xi(t)$ represents the actual shape of the temperature pulse measured by the thermocouple (ΔT_{exp} being the mean temperature increment induced by the HD), the assumption of splitting the energy uniformly into n_r activated rings at once is implicitly made. Therefore, the energy delivered by each heated ring reads

$$\frac{T'_{\mathrm{HD}_j}}{T} = \xi(t)\frac{\Delta T_{exp}}{n_r\, T} \tag{4}$$

One last parameter needs to be defined: the energy provided by each HD q_j'. This energy has been introduced in the above balance equations (equations (2a)–2(c))) as an entropy perturbation source term. With the assumption of an isobaric entropy perturbation as done by Huet and Giauque,[24] $q_j' = s'_{\mathrm{HD}_j}/c_p$ can be expressed as a sole temperature perturbation, for which a delay τ_j can been introduced to take into account the ignition sequence of the HD in the subsonic test case

$$q_j' = \frac{s'_{\mathrm{HD}_j}}{c_p} \equiv \sigma_{\mathrm{HD}_j} = \frac{T'_{\mathrm{HD}_j}}{T}\exp(\mathrm{i}\omega\tau_j) \tag{5}$$

where ω is the angular frequency.

From this input, the entropy wave σ_{HD} generated by the whole HD at the inlet of the nozzle is described as the summation of the entropy waves σ_{HD_j} generated by the individual rings, and recast into

$$\sigma_{\mathrm{HD}} = \sum_{j=1}^{n_r}\frac{T'_{\mathrm{HD}_j}}{T}\exp\left[-\mathrm{i}\omega\left(\frac{L_{j,1}}{c_0 M_0} - \tau_j\right)\right] \tag{6}$$

where $L_{j,1} = x_{N_{in}} - x_{\mathrm{HD}_1} - (j-1)\Delta x_r$ represents the distance from the jth ring to the inlet of the nozzle $x_{N_{in}}$. c_0 is the speed of sound.

3.2. Results

The subsonic case of Bake et al.[8] (case 2) is only studied here using the above analytical approach including the ignition sequence and the number of rings of the HD as the supersonic case (case 1) has been studied in details with success by Leyko et al.[9] The ignition sequence applied in the subsonic test case activates each heating ring one after the other, starting by the one located at the axial position x_{HD_1}. The delay between each ring activation corresponds to the time that one temperature front takes to reach the next ring. Therefore, it can be simply written for each jth ring as

$$\tau_j = -(j-1)\frac{\Delta x_r}{c_0 M_0} \tag{7}$$

so equation (6) can be reduced to

$$\sigma_{\mathrm{HD}} = \xi(t)\frac{\Delta T_{exp}}{T}\exp\left[-\mathrm{i}\omega\left(\frac{x_{N_{in}} - x_{\mathrm{HD}_1}}{c_0 M_0}\right)\right] \tag{8}$$

which is the same expression as the compact expression for the most upstream heated ring (x_{HD_1}). Moreover, since the HD can be considered as compact for acoustics (as shown in the supersonic case), it can be modeled as a compact element located at the axial position x_{HD_1}. The relaxation coefficients τ_1 and τ_2 are chosen to fit at best the experimental measurement of the vibrometer. In Figure 2, the temperature fluctuation modeled analytically is compared with the experimental measurement as well as with the results published in Duran et al.[11] at the vibrometer position $x_{vib} = -58.5$ mm. Note that, at the time, Duran et al. did not study in detail the HD and located it at the axial position $x_{\mathrm{HD}_{Duran}} = -100$ mm, which induces a time delay of 3.6 ms in the signals. Temperature and pressure signals have therefore been shifted by 3.6 ms for proper comparisons of the temperature fluctuation profiles.

Pressure fluctuations issued by the improved temperature hot slug are shown in Figure 3 for three inlet reflection coefficients $R_{in} = [-1, 0, 1]$. Comparisons are made between the analytical compact theory in Duran et al.,[11] the analytical non-compact invariant method in Duran and Moreau,[22] Euler simulations in Duran et al.,[11] and the experimental pressure traces.

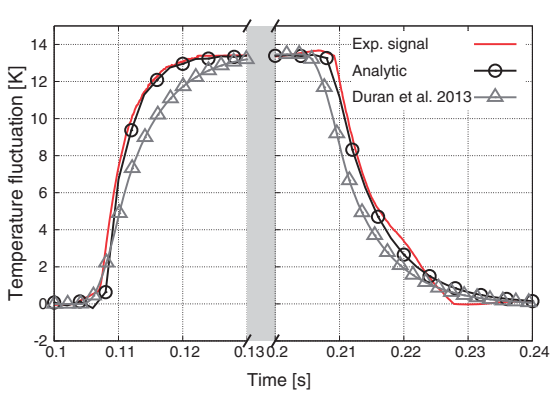

Figure 2. Temperature fluctuation produced by the heating device extracted at the vibrometer position $x_{vib} = -58.5$ mm. Parameters of the model: $\Delta T_{exp} = 13.4$ K, $n_r = 1$, $\tau_1 = 3.5$ ms, $\tau_2 = 7$ ms, $t_0 = 0.1$ s, and $T_p = 0.1$ s.

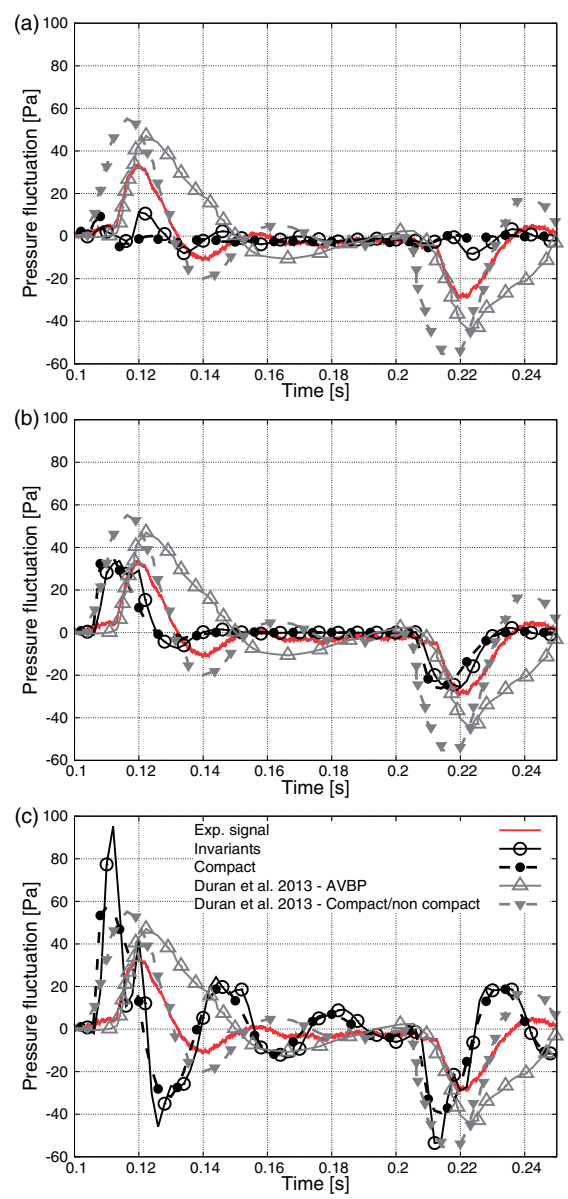

Figure 3. Pressure traces recorded at the outlet of the EWG ($x_{out} = 2100$ mm) for different inlet reflection coefficients R_{in} and a partially reflecting outlet reflection coefficient R_{out} ($K_{out} = 160\,\mathrm{s}^{-1}$). (a) $R_{in} = -1$. (b) $R_{in} = 0$. (c) $R_{in} = 1$.

Very different results are obtained and it should be stressed that for reflection coefficients different from zero ($R_{in} \neq 0$), the pressure fluctuations obtained with the non-compact transfer functions differ from the ones obtained with the compact transfer functions. For $R_{in} = -1$, the nozzle is not compact at this operating point, which disagrees with the results found by Duran et al.[11] Yet, Duran et al.[11] considered partially reflective inlet and outlet boundary conditions (R_{in} close to 1), for which compact and non-compact results are almost the same. The results obtained by Duran et al.[11] can then be retrieved by taking their inlet and outlet relaxation coefficients. Therefore, the large variance in the results shows the great dependence of the generated pressure fluctuations on the unknown inlet impedance and on the temperature–pulse shape.

3.3. Summary

Results show that the HD may be considered as compact for acoustics, and when no time delay τ_j between the heating rings is considered, the overall entropy front is smoothed by the convective process taking place when each front is transported from its origin to the next heating ring. Two parameters are found to strongly modify the generated noise induced by the temperature fluctuation and the ratio of direct and indirect combustion noise: the shape of the hot slug (modulated by the relaxation parameters τ_1 and τ_2) that controls the peak pressure generated, and the inlet reflection coefficient that modifies the shape of the generated acoustic pressure signal. This inlet reflection coefficient, linked to the relaxation chamber upstream of the inlet duct of the EWG seems to be close to -1, and a partially reflective condition seems sufficient to better recover the experimental variation of the noise peak pressure at the outlet of the EWG. Yet, the two improvements brought to previous analytical predictions by Duran et al.[11] do not help bring the pressure peaks closer to experiment, which justify the detailed numerical investigation presented in the next section.

4. EWG numerical simulations

This analytical study of the EWG test cases allowed to assess the influence of different parameters in the transmitted entropy noise. However, the analytical results of the subsonic test case have not shown satisfactory comparisons with experiment yet. Therefore, in order to gain a better insight in the generation and propagation of indirect combustion noise, the subsonic test case at a nozzle-throat Mach number of 0.7 has been simulated by compressible LES of the full 360° EWG configuration in the following subsections.

4.1. Numerical set-up

Considering the whole EWG configuration as shown in Figure 1 without a model describing the honeycomb flow straightener, big vortical structures are detached from the disc and generate unwanted acoustic perturbations. Therefore, the complexity of the flow inside the settling chamber, the lack of model to represent the honeycomb, and the uncertainty issued by the corresponding upstream acoustic reflection coefficient, inferred to trim the settling chamber from the numerical domain. Four numerical meshes were created and then used to study the indirect combustion noise generation within the EWG nozzle flows. A coarse mesh (M0) was used for Euler calculations (not shown here). A medium mesh (M1) was used to reproduce the experiment carried by Bake et al.[8] with wall laws (maximum dimensionless distance to the wall y^+ of about 35 and 20 on average). A finer mesh (M2) was then used to compute nozzle transfer functions on a reduced mesh without wall laws (maximum y^+ of about 20 and 5 on average) and a very fine mesh (M3) intended to yield reference wall-resolved simulations (maximum y^+ below 5 and on average 1 on all walls). M0, M1, and M3 cover the entire EWG configuration, from the inlet of the upstream duct ($x = -250$ mm) to the outlet of the downstream duct ($x = 2100$ mm). Since the computation of the transfer functions of the nozzle does not require to mesh the entire EWG configuration, the domain considered is smaller (from $x = -100$ mm to $x = 400$ mm). All Navier–Stokes (NS) meshes are hybrid composed of prisms at the walls to improve the resolution of the flow boundary layers and tetrahedral elements elsewhere. M0 has only ≈490 k tetrahedral cells (≈145 k nodes). M1 is composed of ≈6 M cells (≈1.5 M nodes) with four prism layers, M2 ≈22 M cells (≈5.4 M nodes) with five prism layers, and M3 contains ≈300 M cells (≈80 M nodes) with six prism layers. The different numerical domains and associated NS meshes are illustrated in Figure 4. They provide a gradual increase of mesh density and prism layer to properly assess the grid influence on the results compared with the initial M0 mesh used in previous studies, which could not resolve any boundary layer and viscous effects properly.

The simulations in this domain are achieved with the LES compressible solver AVBP,[25] and the third-order two-step Taylor–Galerkin numerical scheme TTGC, which allows to control numerical dissipation and dispersion with eight points per wavelength. Within this high-order framework, the AVBP capability to compute acoustics in complex geometries has been demonstrated, for example by Truffin and Poinsot[26]; Martin et al.[27]; Selle et al.[28] to study acoustic instabilities or by Giret et al.,[29,30] Fosso Pouangué et al.[31] and Salas and Moreau[32] in aeroacoustic problems. For all the present

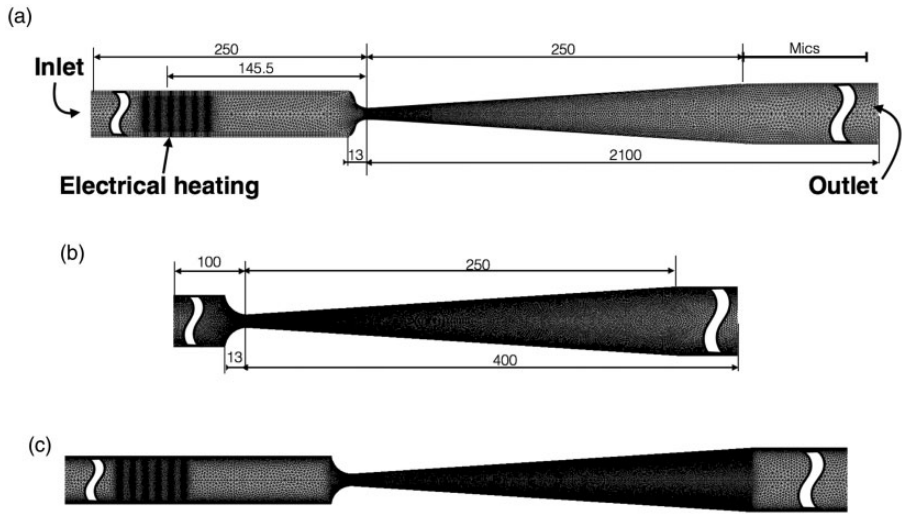

Figure 4. Numerical grids for the baseline flow of the EWG. (Distances indicated in millimeters). (a) M1: Medium mesh. (b) M2: Fine mesh. (c) M3: Very fine mesh.

simulations, the sub-grid scale model is the Wall-Adapting Local Eddy-viscosity model.[33]

Boundary conditions are crucial for acoustic predictions. In the studies of thermo-acoustic instabilities in combustion chambers, the propagation of acoustic and entropy waves through the inlet and the outlet of the combustion chamber determines the coupling of acoustics and the flame, producing or not an unstable mode. At these inflow/outflow boundary conditions, Navier–Stokes Characteristic Boundary Conditions (NSCBC) are thus used to decompose flow variables into ingoing and outgoing waves and to minimize reflections.[34] For the baseline flow, an NSCBC mass-flow rate has been imposed at the inlet to agree with experimental data. To be able to impose a fully reflective inlet, this has been replaced by a total pressure NSCBC condition for the forced case.[35] An inlet relaxation $K_{in} = 50{,}000\,\mathrm{s}^{-1}$ is then imposed.[36] For both configurations, an NSCBC static pressure is imposed at the outlet with an outlet relaxation parameter $K_{out} = 160\,\mathrm{s}^{-1}$ as was used by Leyko et al.[9] to match the experimental impedance. For M1, this pressure has been raised to recover the operating condition at the nozzle throat ($M_{N_{th}} = 0.7$), which accounts for the lack of grid resolution to properly capture the downstream pressure drop. For all NS simulations, no-slip adiabatic boundary conditions (with possibly wall laws) are applied on all walls.

4.2. HD modeling

Leyko et al.,[9] Muhlbauer et al.,[12] and Lourier et al.[13] have proposed different models to describe the HD of the experiment. Usually the model consists of the introduction of a volumetric power source term in the energy equation. In this expression, the source term $\dot{Q}$ is the result of the product of one temporal shape function $\xi(t)$ and a spatial shape function $\phi(x)$ (in the above analytical model, only the temporal function is used). In order to take into account the gap between the heating wires and the duct wall, another function $\varphi(r)$ is introduced here to restrain the energy deposition to a cylinder of radius R_{dep}. Furthermore, each heating module is activated one after the other with a delay corresponding to the convective time of the flow for a distance equal to the module-separation distances (8 mm). Hence, the model of $\dot{Q}$ proposed here to describe the HD reads

$$\dot{Q}(x,r,t) = \frac{E_0}{n_r}\sum_{j=1}^{n_r}\frac{\phi_j(x)\cdot\varphi(r)\cdot\xi_j(t)}{\int\int\int_{-\infty}^{\infty}\phi_j(x)\cdot\varphi(r)\mathrm{d}V\int_0^{\infty}\xi_j(t)\mathrm{d}t} \tag{9}$$

$$\phi_j(x) = \frac{1}{2}\left[1+\tanh\left(\frac{x-x_j+L_j}{d}\right)\tanh\left(\frac{x_j-x+L_j}{d}\right)\right] \tag{9a}$$

$$\xi_j(t) = \begin{cases} 0 & \text{if } t < t_j \\ 1-\exp\left(-\frac{t-t_j}{\tau_1}\right) & \text{if } t \in [t_j;\, t_j+T_p] \\ \phi(t_j+T_p)\exp\left(-\frac{t-t_j-T_p}{\tau_2}\right) & \text{if } t > t_j+T_p \end{cases} \tag{9b}$$

$$\varphi(r) = \begin{cases} 1 & \text{if } r \in [0;\, R_{dep}] \\ 0 & \text{if } r > R_{dep} \end{cases} \tag{9c}$$

where x_j and t_j are the position and the triggering time of the jth heating ring respectively; E_0 is the total energy introduced by the model; L_j is the half-length

of a heating ring n the axial (x) direction; τ_1 and τ_2 are the relaxation times of the temporal function ξ_j; and d is the characteristic slope of the spatial function ϕ. Here, t_j is controlled by a time delay $\Delta\tau$ in the activation of each ring: $t_j = t_0 + (j-1)\Delta\tau$. Note that equation (9b) is the same as the one used in for the analytical modeling (equation (3)), but the activation time corresponding to each heating module t_j is directly taken into account in the expression. This model of energy deposition is generic and reproduces (1) the energy deposition of Leyko et al.[9] and Duran et al.[11] where all the energy is deposited into a single cylinder that covers the entire length covered by all the heating rings and (2) the model of Lourier et al.[13] where the energy is distributed in six different heating modules, each zone being activated at a different instant (the delay being based on the convective time of the mean flow).

The energy E_0 introduced in the simulation comes from the conservation of energy and reads

$$E_0 = \dot{m} c_p \Delta T_{bulk}\left[T_p + (\tau_2 - \tau_1)\left(1 - \exp\left(-\frac{T_p}{\tau_1}\right)\right)\right] \tag{10}$$

where the bulk temperature, velocity, pressure, and Mach number are defined as

$$2T_{bulk}(x) = \frac{\iint_S U_x(r)T(x,r,\theta)r\ dr\ \mathrm{d}\theta}{S\ U_{bulk}} \tag{11a}$$

$$U_{bulk} = \frac{\iint_S U_x(r)\ r\ dr\ \mathrm{d}\theta}{S} \tag{11b}$$

$$P_{bulk}(x) = \frac{\iint_S p(x,r,\theta)\ r\ dr\ \mathrm{d}\theta}{S} \tag{11c}$$

$$M_{bulk}(x) == \frac{U_{bulk}}{\sqrt{\gamma r T_{bulk}(x)}} \tag{11d}$$

with S the duct cross section. U_x is the axial velocity. r is the air specific gas constant.

Two energy deposition shapes have been studied here: the one derived by Leyko et al.,[9] called "Block model" and the one proposed here termed "Delayed model." The main differences between both energy depositions are:

Block: The energy is deposited within a unique cylinder that overlaps the six heating wire modules activated at the same time. The difference with Leyko et al.'s model is that the volume of deposition is restrained by the actual radius of the rings, $R_{dep} = 13.2$ mm (smaller than the duct), to account for the boundary layers present in the LES and not in the Euler computation of Leyko et al..

Table 1. List of parameters for each deposition model test case.

Parameter	Block	Delayed
n_r	1	6
E_0	16.24 J	16.24 J
x_0	−125.5 mm	−145.5 mm
Δx_r	0 mm	8 mm
$2L_j$	40 mm	1 mm
R_{dep}	13.2 mm	13.2 mm
d	1 μm	1 μm
t_0	0.1 s	0.1 s
$\Delta\tau$	0 s	0.702 ms
T_p	0.1 s	0.1 s
τ_1	3.5 ms	3.5 ms
τ_2	7 ms	7 ms

Delayed: The energy is spread over six cylinders of length $L_j = 1$ mm, and a time delay of activation $\Delta\tau = 0.702$ μs between each cylinder is introduced to closely reproduce the experimental ignition sequence.

According to equation (9), the values of the different parameters of the deposition model for the two different test cases are listed in Table 1.

4.3. Reference LES

To assess the quality of the LES and their dependence on the selected grids, bulk quantities as defined in the previous section (equations (11a)–(11d)) are first compared with the isentropic quasi-1D theory. To do so, a time average followed by a surface average of the LES flow fields are calculated in the entire computational domain. Figure 5 shows three baseline flow axial evaluations obtained with the different meshes. As expected, the Euler results on M0 agree well with the isentropic quasi-1D theory for all variables. All simulations also exhibit the same evolution of Mach number and static temperature through the nozzle. Noticeably, all bulk Mach numbers at the nozzle throat (main target) agree with the experimental value, within the experimental uncertainty related to the indirect measuring technique. A similar behavior is also observed on the bulk velocity. Only the bulk pressure evolution is different as the outlet pressure on M1 and M2 has been adjusted to match the operating point on these meshes to compensate either the lack of resolution at the throat or the shorter domain. No correction at the outlet has been applied on M3, which uses the experimental atmospheric pressure. Finally, the results on M3 slightly differ at the throat because of the higher local

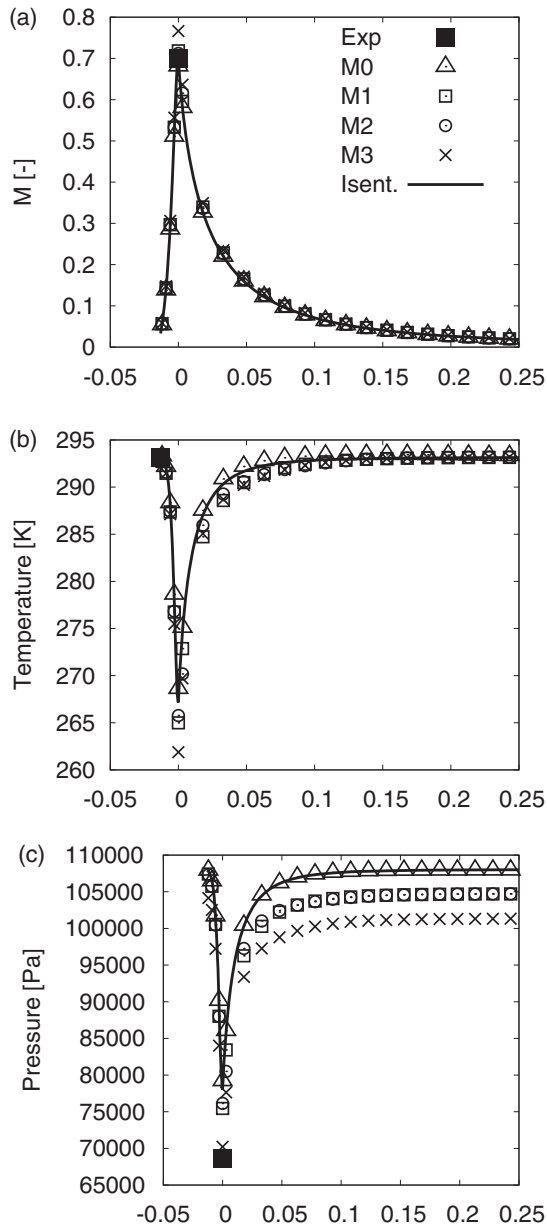

Figure 5. Bulk quantities computed from the LES and compared with the isentropic theory. (a) Bulk Mach number. (b) Bulk temperature. (c) Mean pressure.

resolution and depart from the isentropic values because of the proper capture of the transition to turbulence and the consequent losses. Nevertheless, all grids predict a local transition to turbulence close to the throat and an attached flow (nonzero wall shear stress) in the diverging section as in the experiment.

The main mean values in the simulations and the experiment are also summarized in Tables 2 and 3, respectively. The former provides the experimental and the isentropic theoretical values. The latter gather all simulation results. They are in overall good

Table 2. Comparison of parameters of the unperturbed flow between the numerical simulation and the experiment—Part 1.

Parameter	Experiment	Isentropic
Mass–flow rate $\dot{m}$ (kg/h)	37	37
Total pressure p_t (Pa)	105,640	108,025
Nozzle pressure $p_{N_{th}}$ (Pa)	68,650	78,050
Outlet pressure p_o (Pa)	101,300	100,800
Uptream bulk velocity U_i (m/s)	11.39	11.33
Nozzle Mach number $M_{N_{th}}$	0.7	0.7

Table 3. Comparison of parameters of the unperturbed flow between the numerical simulation and the experiment—Part 2.

Parameter	Euler (M0)	LES (M1)	LES(M2)	LES(M3)
$\dot{m}$ (kg/h)	37	37	37	37
p_t (Pa)	108,327	107,840	107,730	104,620
$p_{N_{th}}$ (Pa)	75,762	69,100	71,900	66,640
p_o (Pa)	100,800	104,700	104,715	101,300
U_i (m/s)	11.31	11.34	11.34	11.67
$M_{N_{th}}$	0.70	0.72	0.685	0.725

agreement. In particular, the simulation on M3 yields values of total and static pressure that are the closest to the measurements. Noticeably, the prediction of the total pressure at the nozzle throat that indicates the local losses is greatly improved on M3. Again all targeted nozzle-throat Mach number are within the experimental uncertainty. The low variability in the isentropic vs bulk profiles shown in Figure 5 as well as the good comparison with the experimental measurements of Tables 2 and 3 show that the operating point has been correctly retrieved in all LES.

Additional quantitative comparisons can be obtained by looking at radial profiles of time- and azimuthally-averaged flow properties along the EWG nozzle. Two representative positions are selected here, at the nozzle throat ($x_{N_{th}} = 0\,\text{mm}$) and at the nozzle-diffuser outlet ($x_{N_{out}} = 250\,\text{mm}$). Only the Mach number and the temperature are shown as they are representative of the kinematics and the thermal state of the flow. Similar behaviors are found on velocity and pressure for instance.

Profiles of Mach number and temperature at these two locations are shown for all NS simulations in Figures 6 and 7, respectively. They are found very similar for all computations. Up to the nozzle all profiles of Mach number are identical. The latter then increases significantly up to the nozzle throat where the acceleration of the flow is the strongest and the boundary layer the thinnest. Its thickness seems to be well captured in

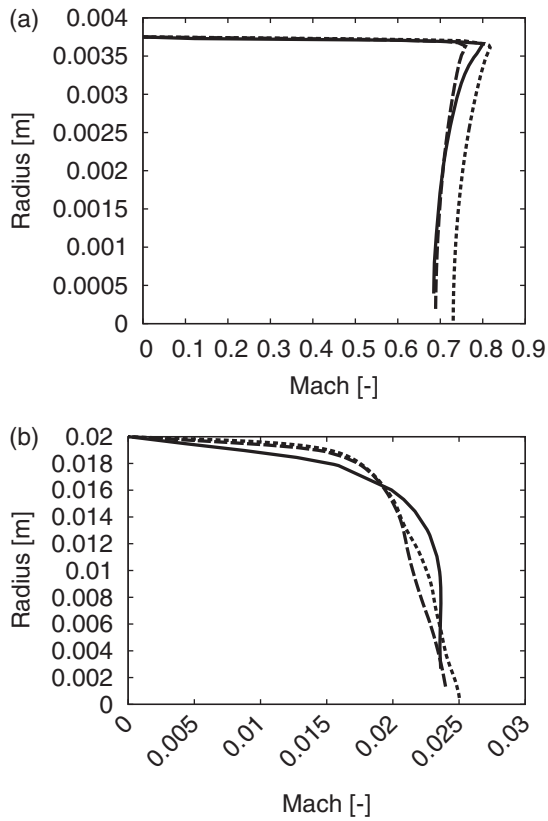

Figure 6. Temporal and azimuthal average of the Mach number versus the radius. M1 (——). M2 (– – –). M3 (- - -). (a) Nozzle-throat $x_{N_{th}} = 0.0$ mm. (b) Outlet of the nozzle diffuser $x_{N_{out}} = 250$ mm.

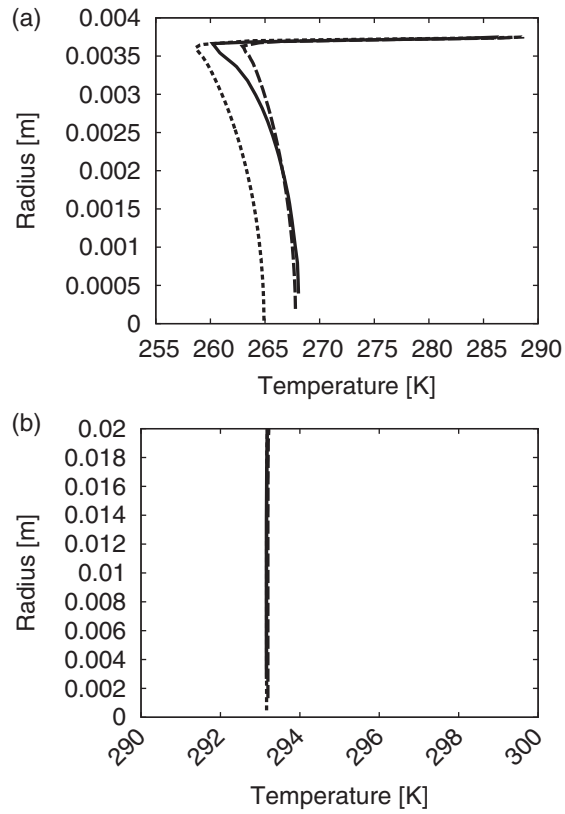

Figure 7. Temporal and azimuthal average of the temperature versus the radius. M1 (——). M2 (– – –). M3 (- - -). (a) Nozzle-throat $x_{N_{th}} = 0.0$ mm. (b) Outlet of the nozzle diffuser $x_{N_{out}} = 250$ mm.

all three simulations, but a stronger acceleration along the axis is seen on M3, even though the reached Mach number remains within the uncertainty of the experimental target (Figure 6(a)). Because of the adverse pressure gradient in the diffuser, the boundary layer thickens up to the outlet. The same final boundary layer thickness is reached on the finest meshes M2 and M3 (Figure 6(b)). Only on M1 the boundary layer is thicker due to the grid resolution. Similar low Mach numbers of about 0.022 are reached on the centerline for all three simulations. The evolution of the temperature is also similar in all simulations up to the nozzle. A decrease of temperature is then seen up to the nozzle throat as a consequence of the above flow acceleration. The thermal boundary layer thickness at the nozzle throat seems to be the same for all three calculations (Figure 7(a)). Due to the stronger acceleration on M3, a lower temperature is reached locally. Yet the same temperature value is retrieved at the exit of the nozzle (Figure 7(b)). Moreover, the largest radial variations of temperature and consequently of pressure are found in the nozzle-throat region because of the larger curvature of the streamlines at this specific location. As a result, *an unsteady* azimuthal velocity is induced in the diverging section, which can be explained by the local radial equilibrium equation (already used in the experiment to compute the nozzle Mach number[23,37]

$$\frac{\partial p}{\partial r} \simeq -\rho \frac{u_\theta^2}{r} \tag{12}$$

This equation stands for the momentum conservation in the radial direction for an axisymmetric flow without radial velocity, which is only strictly valid at the throat. Yet, the radial velocity remains small in the present slowly-varying divergent. Note also that the mean tangential velocity remains zero in the present axisymmetric setup. The generation of u_θ means that vorticity is generated in the axial and radial directions (ξ_x and ξ_r, respectively) by the radial pressure gradient. Such vortices are then stretched and deformed by the flow acceleration through the nozzle and is a sound generation mechanism that contributes to the indirect noise generation.

Overall, it can be concluded that all simulations capture the targeted operating condition and have a very

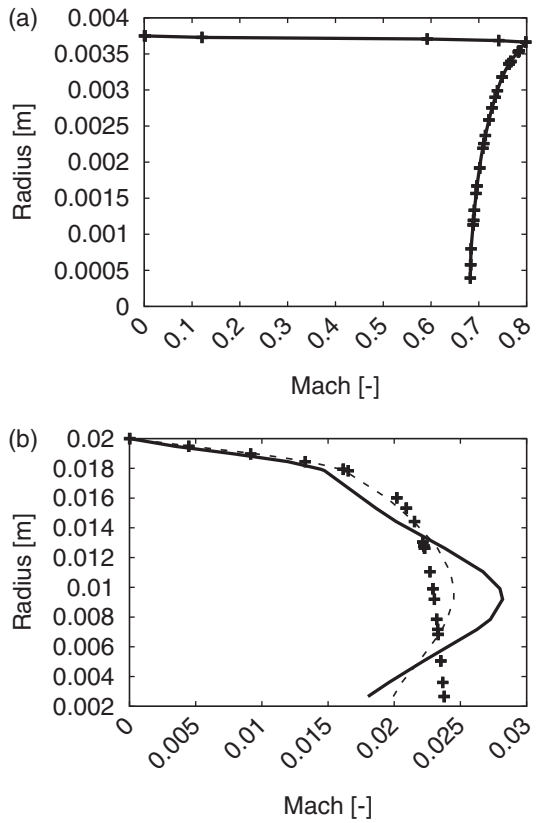

Figure 8. Azimuthal average of the Mach number versus radius. Baseline flow simulation on M1 (+++). $t_1 = 0.1$ s—beginning of the energy introduction (——). $t_2 = 0.2$ s—end of the energy introduction (– – –). (a) Nozzle-throat $x_{N_{th}} = 0.0$ mm. (b) Outlet of the nozzle diffuser $x_{N_{out}} = 250$ mm.

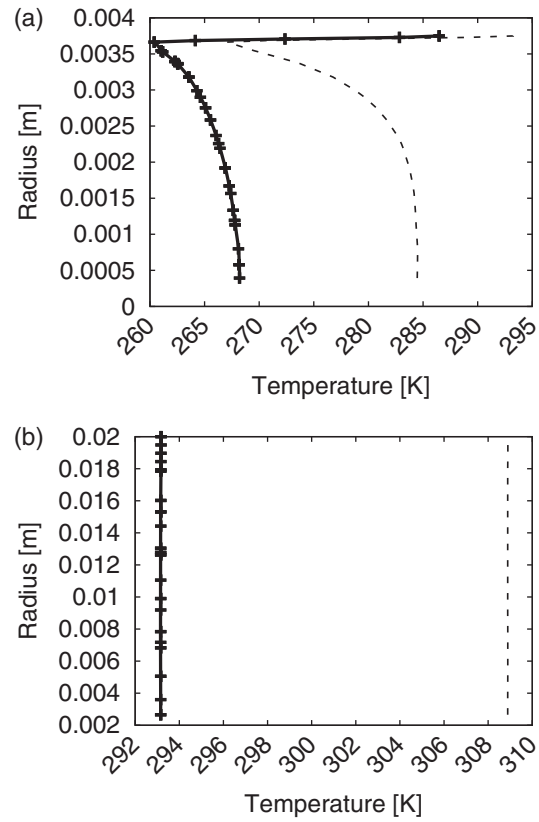

Figure 9. Azimuthal average of the temperature versus radius. Baseline flow simulation on M1 (+++). $t_1 = 0.1$ s—beginning of the energy introduction (——). $t_2 = 0.2$ s—end of the energy introduction (– – –). (a) Nozzle-throat $x_{N_{th}} = 0.0$ mm. (b) Outlet of the nozzle diffuser $x_{N_{out}} = 250$ mm.

similar flow development. Therefore, parametric simulations with various energy-deposition models have been performed on the medium grid M1.

4.4. Simulation results with HD

The influence of the energy deposition model is first shown on the Mach number and the temperature in Figures 8 and 9. Similar evolutions are seen on the axial velocity and pressure for instance. The instantaneous profiles are extracted at two different instants ($t_1 = 100$ ms and $t_2 = 200$ ms) of the "Delayed model" simulation, and compared with the mean profiles extracted from the baseline flow simulation without heating. t_1 corresponds to the time when the deposition starts and t_2 when the energy deposition stops. All profiles from the inlet of the nozzle ($x_{N_{in}}$) to the nozzle throat ($x_{N_{th}}$) are found to be equivalent at t_1 to the mean profiles from the baseline flow simulation. This is due to the fact that the flow is mostly laminar without much perturbation before the nozzle throat. In the diverging section though, the unsteadiness introduced by the transition to turbulence and the growing turbulent boundary layer caused by the adverse pressure gradient is clearly visible in the instantaneous solution profiles. For instance, a large variation of the Mach number instantaneous profiles at the outlet of the nozzle diffuser in Figure 8(b) is caused by the jet flapping. Profiles at t_2 show the evolution of the different variables when the temperature is increased by the energy deposition. The 13.4 K increase of temperature measured in the upstream duct is not enough to modify the Mach number profiles significantly. However, this temperature increase is noticeable in the pressure profiles (pressure increase by about 20 Pa) as shown in Figure 10. A thickening of the thermal boundary layer is also seen in the temperature profiles at the throat (Figure 9(a)). It is worth noting that at the chosen instants, there is no sound generation by the entropy wave: at t_1 the hot slug has not reached the nozzle and at t_2, the first temperature front has already traversed the nozzle generating a steady state after its passage (the temperature between t_1 and t_2 reaching a constant value). Therefore, observed pressure fluctuations are only the result of boundary condition reflections and vortex sound.

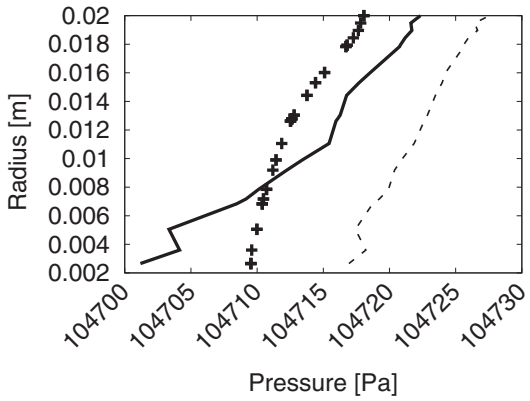

Figure 10. Azimuthal average of the static pressure versus radius at the outlet of the nozzle diffuser ($x_{N_{out}} = 250$ mm). Baseline flow simulation on M1 (+++). $t_1 = 0.1$ s—beginning of the energy introduction (——). $t_2 = 0.2$ s—end of the energy introduction (– – –).

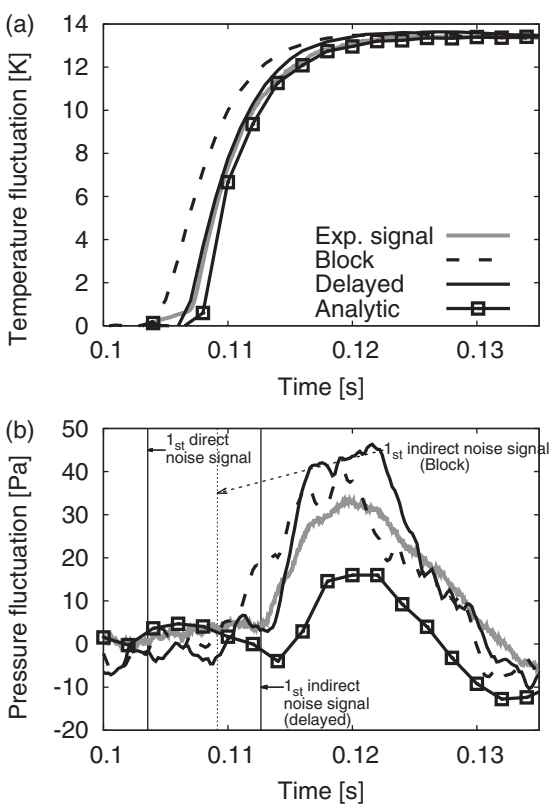

Figure 11. LES with heating device. Temperature and pressure traces generated by the introduction of a hot slug by the inlet boundary condition. (a) Temperature fluctuation at the vibrometer position ($x_{vib} = -58.5$ mm). (b) Pressure fluctuation at the fourth microphone $x_{mic_4} = 1150.5$ mm).

The first instants of the energy deposition are compared with the experimental measurements. To do so, only the first 35 ms of the energy deposition are shown in Figure 11, where the mean temperature and pressure traces obtained in the numerical simulations are compared with the analytical results (shown above for the invariants with $R_{in} = -1$ in Figure 3(a)) and the experimental data. As already highlighted in the analytical evaluation of the EWG, the simultaneous activation of all the heating rings (block deposition model) induces a time difference in the temperature and pressure signals of about 3 ms due to the convection time of the temperature front between each heating ring. This time delay is taken into account in the delayed model, and is computed using the values reported by Bake et al.,[8] namely the bulk velocity in the upstream duct $U_{bulk} \approx 11.4$ m/s and the spacing between each heating ring $\Delta x_R = 8$ mm. A total time delay is found to be about 3.5 ms. Figure 11(a) shows the temperature evolution at the vibrometer position. The two delayed energy deposition models show a very good agreement with the experimental signal. Therefore, the parameters chosen to describe the hot slug shape with the delayed model reproduce the shape of the temperature fluctuation measured by the vibrometer well, and the delay of activation of each heating module as well as the right convection velocity of the hot slug provides the correct operating point (the hot slug arrives at the correct time at the vibrometer position). This also agrees with the numerical results of Lourier et al.[13] that computed the time difference of different noise sources (direct and indirect noise). As Lourier et al.[13] has already found, the first direct noise signal (noise produced by the fluctuating heat release of the HD) starts at about 4 ms after the triggering of the energy deposition and the first indirect noise signal (due to the acceleration of the hot spot through the nozzle) arrives at about 12.5 ms. The present pressure fluctuations generated by the heating and convection of the hot slug through the nozzle are shown in Figure 11(b) at the fourth microphone position ($x_{mic_4} = 1150.5$ mm), where time delays computed by Lourier et al. are also presented. The HD is found to be compact for the acoustic waves of interest and direct noise signals should then arrive at the same time for both deposition models ($t \approx 103.5$ ms). Indirect noise contribution is seen to start earlier for the block deposition model (about 3.5 ms earlier) compared with the delayed model. Therefore, between $t \approx 103.5$ and $t \approx 109.1$ ms, only direct noise is measured by the microphone. Because of the short simulation time and the consequent small window of time for purely direct noise contribution, one cannot conclude which deposition model produces more or less direct noise. Nevertheless, the overall noise produced by the block deposition model is clearly more spread and

reaches a lower peak value (same amount of energy introduced by both models). Furthermore, when comparing the numerical delayed-model pressure signal with the analytical one, the shape of both signals is very similar (Figure 11(b)) and the starting point of indirect noise signals matches very well (slightly after Lourier et al.[13] prediction). In the zone where direct and indirect noise interact together, the analytical model appears to underestimate the pressure signal by half when LES seems to overestimate only the peak value, obtaining a better agreement with the experimental measurement. The differences between the analytical and numerical pressure signals can be mostly attributed to the turbulent vortices produced in the diffuser and the consequent produced vortex sound, and the possible excitation of the nozzle jet by the entropy disturbance.

4.5. Simulation results without HD

Another LES has been achieved on M1, in which a temperature fluctuation with the same characteristics as the ones generated by the HD is introduced in the domain without the generated direct noise. To estimate the amount of indirect noise generated in the LES, a plane next to the HD ($x = -100$ mm) is extracted from the forced simulation discussed above to obtain a 2D temperature field that depends on time only, and that is imposed at the inlet boundary condition. Figure 12 compares the result of this simulation with the delayed deposition model and the experimental results. The temperature and pressure fluctuations without HD have been shifted by 10 ms (convection time of the flow to reach the HD) to make a fair comparison. The temperature fluctuations show an attenuation of the maximum value caused by the longer path followed by the hot slug to reach the nozzle. Despite the smaller maximum temperature fluctuation, pressure traces indicate that the amount of indirect noise generated is almost the same as the overall contribution of both noise sources, indicating that direct noise has a very small contribution and that indirect noise generation is the dominant source in this experiment as previously found by Lourier et al.[13]

4.6. Deformation of the entropy spot

As mentioned above, the bulk temperature given by equation (11a) is energy conservative by construction and should therefore be considered to verify if the entropy fluctuations only suffer from dispersion and not dissipation through the EWG nozzle. Such a property has already been verified by Morgans et al.[14] and Giusti et al.[15] for constant section turbulent channels flows. To look at the time evolution of the temperature

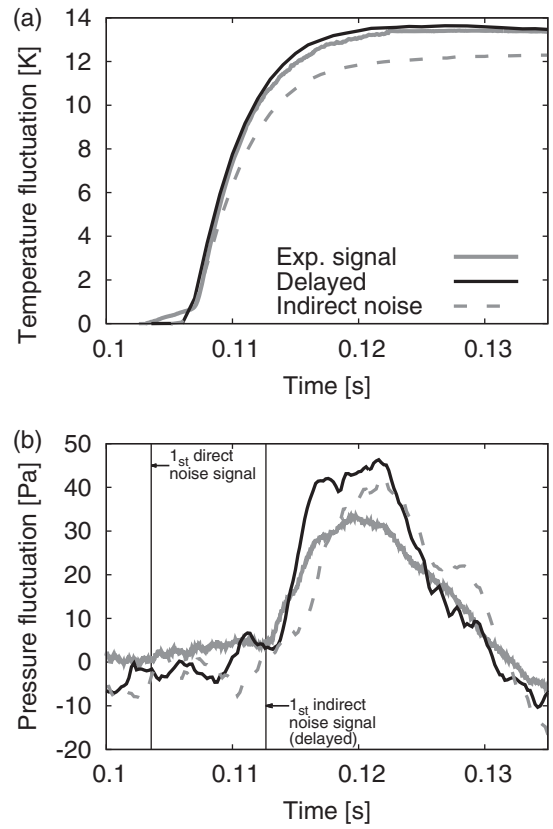

Figure 12. LES without heating device. Temperature and pressure traces generated by the introduction of a hot slug by the inlet boundary condition. (a) Temperature fluctuation at the vibrometer position ($x_{vib} = -58.5$ mm). (b) Pressure fluctuation at the fourth microphone $x_{mic_4} = 1150.5$ mm).

fluctuations, profiles of $T_{dimless}(x) = \frac{(T_{bulk}(x) - \bar{T}_{0,bulk}(x))}{\bar{T}_{0,bulk}(x)}$, where $\bar{T}_{0,bulk}(x)$ is the time-averaged bulk temperature of the baseline flow, are extracted at different axial locations of the domain. Figure 13 shows the evolution of $T_{dimless}$ at the nozzle outlet and $x = 1$ m from the nozzle throat for the two LES and the analytical temperature convection model. The latter is deduced from the 1D Euler energy equation for an adiabatic flow along the nozzle axis, and is given by the system

$$\begin{cases} \frac{\partial T(t,x)}{\partial t} + u(x)\frac{\partial T(t,x)}{\partial x} = \frac{1}{\rho(x)c_p}\left[u(x)\frac{\partial p(x)}{\partial x} + \dot{Q}(t,x)\right] \\ T(t=0,x) = T(x) \end{cases} \quad (13)$$

where $u(x)$, $\rho(x)$, $T(x)$, and $\frac{\partial p(x)}{\partial x}$ are extracted from the isentropic mean flow. The shape of the temperature fluctuation is conserved through the nozzle and its shape is only distorted and attenuated in the downstream duct. The entropy hot slug needs almost one meter for its amplitude to be decreased by the effects of the mean flow. It is important to remember that the temperature fluctuation generated by the EWG HD is

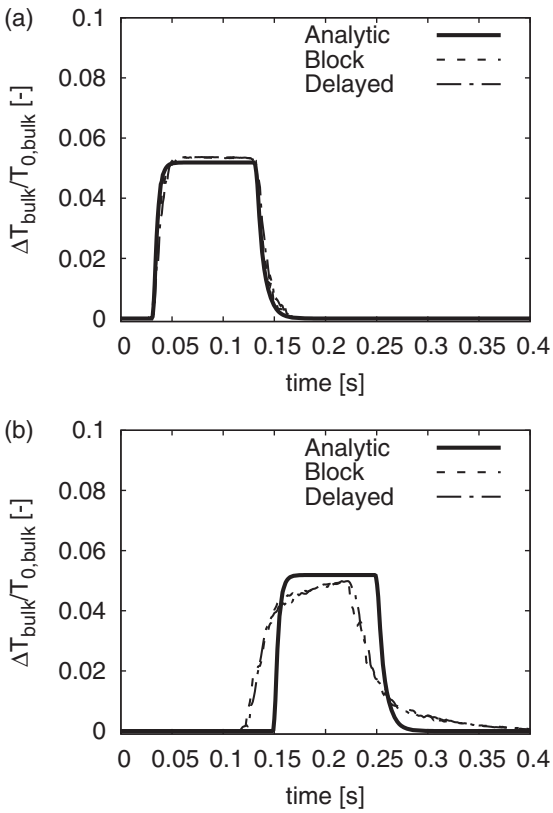

Figure 13. Azimuthal average of the dimensionless bulk temperature $T_{dimless} = (T_{bulk} - T_{0bulk})/T_{0bulk}$ at the different positions of the nozzle against time. (a) Outlet of the nozzle, $x_{N_{out}} = 0.25$ m. (b) $x = 1$ m.

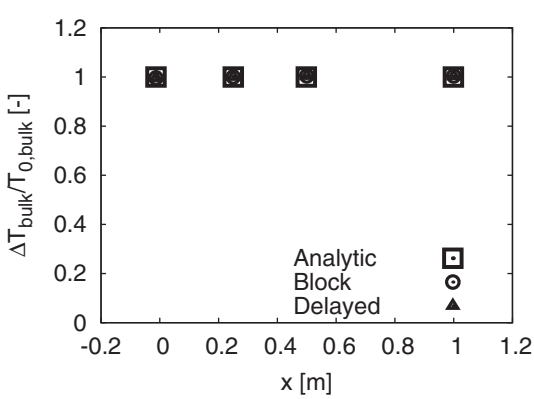

Figure 14. Relative magnitude of $T_{dimless}$ (compared to its value taken at the vibrometer position) as it is convected through the EWG nozzle.

composed of almost only very low frequencies.[8] Even though additional 3D effects are present in the EWG nozzle, this behavior is therefore consistent with the result of Giusti et al.[15] which noticed in a straight duct that the smaller the frequency is, the smaller the dispersion of the entropy perturbation is. In order to estimate the dissipation of the entropy wave through the nozzle, the temporal relative integral (to the vibrometer position) of each extracted position is computed and showed in Figure 14, which clearly shows that the entropy fluctuation is only convected through the nozzle without dissipation.

5. Conclusion

The subsonic operating point of the EWG experiment has been computed by LES. Two energy deposition shapes have been compared to account for the experimental ignition sequence and geometry: the one used by Leyko et al.,[9] and the delayed deposition proposed in this work. The unknown inlet acoustic reflection coefficient is assumed to be fully reflective (most physical choice) to have a fair comparison with the analytical models for a compact nozzle of Duran et al.[11] and for a non-compact nozzle of Duran and Moreau.[22] The time delay between the activation of the heating modules must be considered to retrieve the correct time delay in the temperature signal measured at the vibrometer and pressure signals at the microphones. Furthermore, pressure signal extracted from the LES at the fourth microphone using the delayed ignition model clearly reproduces the experimental signal well, while the analytical analysis did not. Moreover, the temperature fluctuations generated by the delayed ignition model have been introduced in another simulation, which clearly shows that the pressure fluctuations produced by the acceleration of the hot slug yields indirect noise almost entirely as was found by Lourier et al.[13]

Finally, the convection of the hot spot has also been studied, and the detailed turbulent numerical results have been compared with a quasi-1D convection solution of a hot spot, by looking at one dimensional fields of the temperature fluctuations at different instants and locations in the nozzle. As was previously found by Morgans et al.[14] in a direct numerical simulation of a temperature pulse convecting through a turbulent channel, the amplitude and the shape of the entropy spot gets distorted when convecting through the EWG nozzle (the amplitude of the entropy spot decreases and its shape is dispersed), but hardly any dissipation occurs. The attenuation and distortion of the entropy spot in the simulation appear to be negligible through the nozzle and become important only when convected over a long distance in the downstream duct. Moreover since in this EWG experiment, the dominant frequencies of the entropy forcing are very low, the effects of dispersion by the mean flow are weak.

Acknowledgments

The authors gratefully acknowledge all RECORD (Research on Core Noise Reduction) partners for sharing experimental and numerical data, and the funding from the European Union Seventh Framework Collaborative project RECORD

under Grant No. RG66913. The authors are specially thankful to Dr. Friedrich Bake from DLR for providing all the experimental data and Frédérique Duvinage from AllianTech for the complementary informations on transfer functions of the microphones that yielded the experimental unsteady pressure traces.

Declaration of Conflicting Interests

The author(s) declared no potential conflicts of interest with respect to the research, authorship, and/or publication of this article.

Funding

The author(s) received funding from the European Union Seventh Framework Collaborative project RECORD under Grant No. RG66913.

References

1. Ihme M. Combustion and engine-core noise. *Ann Rev Fluid Mech* 2017; 49: 277–310.
2. Nesbitt E. Towards a quieter low pressure turbine: design characteristics and prediction needs. *Int J Aerocoust* 2010; 10: 1–15.
3. Livebardon T. *Modeling of combustion in helicopter engines*. PhD Thesis, Université de Toulouse—Ecole doctorale MEGeP Dynamique des Fluides, Toulouse, France, 2015.
4. Livebardon T, Moreau S, Gicquel LYM, et al. Combining LES of combustion chamber and an actuator disk theory to predict combustion noise in a helicopter engine. *Combust Flame* 2016; 165: 272–287.
5. Thomas A and Williams GT. Flame noise: sound emmission from spark-ignited bubbles of combustible gas. *Proc R Soc Lond A* 1966; 294: 449–466.
6. Marble FE and Candel S. Acoustic disturbances from gas nonuniformities convected through a nozzle. *J Sound Vib* 1977; 55: 225–243.
7. Bake F, Kings N, Fischer A, et al. Experimental investigation of the entropy noise mechanism in aero-engines. *Int J Aerocoustics* 2008; 8: 125–142.
8. Bake F, Richter C, Muhlbauer B, et al. The entropy wave generator (ewg): a reference case on entropy noise. *J Sound Vib* 2009; 326: 574–598.
9. Leyko M, Moreau S, Nicoud F, et al. Numerical and analytical modelling of entropy noise in a supersonic nozzle with a shock. *J Sound Vib* 2011; 330: 3944–3958.
10. Leyko M, Nicoud F, Moreau S, et al. Numerical and analytical investigation of the indirect noise in a nozzle. In: *Proceedings of the summer program*. USA: Center for Turbulence Research, Stanford University, 2008, pp. 343–354.
11. Duran I, Moreau S and Poinsot T. Analytical and numerical study of combustion noise through a subsonic nozzle. *AIAA J* 2013; 51: 42–52.
12. Muhlbauer B, Noll B and Aigner M. Numerical investigation of the fundamental mechanism for entropy noise generation in aero-engines. *Acta Acustica united with Acustica* 2009; 95: 470–478.
13. Lourier JM, Huber A, Noll B, et al. Numerical analysis of indirect combustion noise generation within a subsonic nozzle. *AIAA J* 2014; 52: 2114–2126.
14. Morgans AS, Goh CS and Dahan JA. The dissipation and shear dispersion of entropy waves in combustor thermoacoustics. *J Fluid Mech* 2013; 733: R2 1–11.
15. Giusti A, Worth NA, Mastorakos E, et al. Experimental and numerical investigation into the propagation of entropy waves. *AIAA J* 2017; 55: 446–458.
16. Hosseinalipour SM, Fattahi A, Afshari H, et al. On the effects of convecting entropy waves on the combustor hydrodynamics. *Appl Therm Eng* 2017; 110: 901–909.
17. Papadogiannis D, Wang G, Moreau S, et al. Assessment of the indirect combustion noise generated in a transonic high-pressure turbine stage. *J Eng Gas Turb Power* 2016; 138: 041503 1–8.
18. Wang G, Sanjose M, Moreau S, et al. Noise mechanisms in a transonic high-pressure turbine stage. *Int J Aerocoust* 2016; 15: 144–161.
19. Howe MS. Indirect combustion noise. *J Fluid Mech* 2010; 659: 267–288.
20. Ullrich WC, Gikadi J, Jörg C, et al. Acoustic-entropy coupling behavior and acoustic scattering properties of a laval nozzle. In: *20th AIAA/CEAS aeroacoustics conference*, Atlanta, GA, AIAA Paper 2014-3193, 2014.
21. Ullrich WC, Sattelmayer T, Kings N, et al. Numerical investigation of indirect noise generation by accelerated vorticity. In: *21st AIAA/CEAS aeroacoustics conference*, Dallas TX, AIAA Paper 2015-2382, 2015.
22. Duran I and Moreau S. Solution of the quasi-one-dimensional linearized euler equations using flow invariants and the magnus expansion. *J Fluid Mech* 2013; 723: 190–231.
23. Becerril C, Moreau S, Bauerheim M, et al. Numerical investigation of combustion noise: the entropy wave generator. In: *22nd AIAA/CEAS aeroacoustics conference*, Lyon, France, AIAA Paper 2016-2830, 2016.
24. Huet M and Giauque A. A nonlinear model for indirect combustion noise through a compact nozzle. *J Fluid Mech* 2013; 733: 268–301.
25. Schønfeld T and Poinsot T. Influence of boundary conditions in LES of premixed combustion instabilities. In: *Annual research briefs*. Center for Turbulence Research, NASA Ames/Stanford University, 1999, pp. 73–84.
26. Truffin K and Poinsot T. Comparison and extension of methods for acoustic identification of burners. *Combust Flame* 2005; 142: 388–400.
27. Martin C, Benoit L, Sommerer Y, et al. LES and acoustic analysis of combustion instability in a staged turbulent swirled combustor. *AIAA J* 2006; 44: 741–750.
28. Selle L, Benoit L, Poinsot T, et al. Joint use of compressible large-eddy simulation and Helmholtz solvers for the analysis of rotating modes in an industrial swirled burner. *Combust Flame* 2006; 145: 194–205.
29. Giret J, Sengissen A, Moreau S, et al. Prediction of lagoon landing-gear noise using an unstructured les solver. In: *19th AIAA/CEAS aeroacoustics conference*, Berlin, Germany, AIAA Paper 2013-2113, 2013.
30. Giret J, Sengissen A, Moreau S, et al. Noise source analysis of a rod–airfoil configuration using unstructured large eddy simulation. *AIAA J* 2015; 53: 1062–1076.

31. Fosso Pouangué A, Sanjosé M, Moreau S, et al. Subsonic jet noise simulations using both structured and unstructured grids. *AIAA J* 2015; 53: 55–69.
32. Salas P and Moreau S. Aeroacoustic simulations of a simplified high-lift device accounting for some installation effects. *AIAA J* 2017; 55: 774–789.
33. Nicoud F and Ducros F. Subgrid-scale stress modelling based on the square of the velocity gradient. *Flow Turb Combust* 1999; 62: 183–200.
34. Poinsot T and Lele S. Boundary conditions for direct simulations of compressible viscous flows. *J Comput Phys* 1992; 101: 104–129.
35. Sanjosé M, Fosso Pouangué A, Moreau S, et al. Unstructured les of the baseline exejet dual-stream jet. In: *20th AIAA/CEAS aeroacoustics conference*, Atlanta, GA, AIAA Paper 2014-3037, 2014.
36. Selle L, Nicoud F and Poinsot T. The actual impedance of non-reflecting boundary conditions: implications for the computation of resonators. *AIAA J* 2004; 42: 958–964.
37. Knobloch K, Werner T and Bake F. Noise generation in hot nozzle flow. In: *ASME turbo expo 2015: turbine technical conference and exposition*. American Society of Mechanical Engineers, 2015, pp. V02BT41A012–V02BT41A012.